

<https://doi.org/10.1038/s42005-024-01673-y>

# Discovery of charge order above room-temperature in the prototypical kagome superconductor $\text{La}(\text{Ru}_{1-x}\text{Fe}_x)_3\text{Si}_2$

Check for updates

I. Plokhikh<sup>1,12</sup>, C. Mielke III<sup>2,3,12</sup>, H. Nakamura<sup>4</sup>, V. Petricek<sup>5</sup>, Y. Qin<sup>6</sup>, V. Szagari<sup>2</sup>, J. Küspert<sup>3</sup>, I. Biało<sup>3,7</sup>, S. Shin<sup>1</sup>, O. Ivashko<sup>8</sup>, J. N. Graham<sup>2</sup>, M. v. Zimmermann<sup>8</sup>, M. Medarde<sup>1</sup>, A. Amato<sup>2</sup>, R. Khasanov<sup>2</sup>, H. Luetkens<sup>2</sup>, M. H. Fischer<sup>3</sup>, M. Z. Hasan<sup>9</sup>, J.-X. Yin<sup>10</sup>, T. Neupert<sup>3</sup>, J. Chang<sup>3</sup>, G. Xu<sup>6</sup>, S. Nakatsuji<sup>4,11</sup>, E. Pomjakushina<sup>1</sup>, D. J. Gawryluk<sup>1</sup> ✉ & Z. Guguchia<sup>2</sup> ✉

The kagome lattice is an intriguing and rich platform for discovering, tuning and understanding the diverse phases of quantum matter, crucial for advancing modern and future electronics. Despite considerable efforts, accessing correlated phases at room temperature has been challenging. Using single-crystal X-ray diffraction, we discovered charge order above room temperature in  $\text{La}(\text{Ru}_{1-x}\text{Fe}_x)_3\text{Si}_2$  ( $x = 0, 0.01, 0.05$ ), where charge order related to out-of-plane Ru atom displacements appears below  $T_{\text{CO,I}} \simeq 400$  K. The secondary charge ordered phase emerges below  $T_{\text{CO,II}} \simeq 80\text{--}170$  K. Furthermore, first principles calculations reveal both the kagome flat band and the van Hove point near the Fermi energy in  $\text{LaRu}_3\text{Si}_2$ , driven by Ru- $d_{z^2}$  orbitals. Our results identify  $\text{LaRu}_3\text{Si}_2$  as the kagome superconductor with the highest known charge ordering temperature, offering a promising avenue for researching room temperature quantum phases and developing related technologies.

Charge order is prevalent in materials exhibiting strong electronic correlations and pronounced electron–phonon interactions. This phenomenon is observed in various systems such as cuprate high-temperature superconductors<sup>1–3</sup>, colossal magnetoresistive manganites<sup>4</sup>, transition-metal dichalcogenides (TMDs)<sup>5–7</sup>, and more recently, kagome lattice metals<sup>8,9</sup>. Charge order is usually associated with unconventional quantum phases, which highlights the importance of charge order in understanding and manipulating novel phases of matter. Besides the fundamental aspect, layered quantum materials with charge order have also been widely studied and proposed to be potential candidates for next-generation electronic devices. However, the lack of room-temperature charge-order materials has limited the development of charge-order-based electronic devices. Thus, it is of importance both from fundamental and technological aspects to find more materials with room-temperature charge orders.

Along these lines, several kagome metals<sup>8–17</sup> have appeared as promising platforms to study unconventional correlated quantum phases, including charge order. There are three material classes of kagome lattice systems that were recently shown to exhibit charge order: the  $\text{AV}_3\text{Sb}_5$  ( $A = \text{K, Rb, Cs}$ )<sup>9,18,19</sup> family of materials,  $\text{ScV}_6\text{Sn}_6$ <sup>20–25</sup> and  $\text{FeGe}$ <sup>26–28</sup>.  $\text{AV}_3\text{Sb}_5$  exhibits two correlated orders: charge order below  $T_{\text{CO}} \simeq 80\text{--}110$  K and a superconducting (SC) instability below  $T_c \simeq 1\text{--}3$  K<sup>29–31</sup>. The system  $\text{ScV}_6\text{Sn}_6$  has a similar vanadium structural motif as  $\text{AV}_3\text{Sb}_5$  and exhibits charge order below  $T_{\text{CO}} \simeq 90$  K, however it is not superconducting down to the lowest measured temperature.  $\text{FeGe}$  is a correlated magnetic kagome system and exhibits an A-type antiferromagnetic (AFM) order below 400 K and a charge order below 100 K. The unique features of  $\text{AV}_3\text{Sb}_5$  and  $\text{ScV}_6\text{Sn}_6$  are the emergence of possibly time-reversal symmetry (TRS) breaking chiral charge orders with both magnetic<sup>8,11,21,32–44</sup> and electronic anomalies<sup>45,46</sup>. Theoretically, these features could be explained by a complex

<sup>1</sup>Laboratory for Multiscale Materials Experiments, Paul Scherrer Institut, CH-5232 Villigen, PSI, Switzerland. <sup>2</sup>Laboratory for Muon Spin Spectroscopy, Paul Scherrer Institute, CH-5232 Villigen, PSI, Switzerland. <sup>3</sup>Physik-Institut, Universität Zürich, Winterthurerstrasse 190, CH-8057 Zürich, Switzerland. <sup>4</sup>Institute for Solid State Physics (ISSP), University of Tokyo, Kashiwa, Chiba 277-8581, Japan. <sup>5</sup>Institute of Physics CAS, Na Slovance 1999/2, Praha, Czech Republic. <sup>6</sup>Wuhan National High Magnetic Field Center and School of Physics, Huazhong University of Science and Technology, 430074 Wuhan, China. <sup>7</sup>AGH University of Krakow, Faculty of Physics and Applied Computer Science, 30-059 Kraków, Poland. <sup>8</sup>Deutsches Elektronen-Synchrotron DESY, Notkestraße 85, 22607 Hamburg, Germany. <sup>9</sup>Laboratory for Topological Quantum Matter and Advanced Spectroscopy (B7), Department of Physics, Princeton University, Princeton, NJ 08544, USA. <sup>10</sup>Department of Physics, Southern University of Science and Technology, 518055 Shenzhen, Guangdong, China. <sup>11</sup>Department of Physics, University of Tokyo, 113-0033 Bunkyo-ku, Tokyo, Japan. <sup>12</sup>These authors contributed equally to: I. Plokhikh, C. Mielke III. ✉e-mail: [dariusz.gawryluk@psi.ch](mailto:dariusz.gawryluk@psi.ch); [zurab.guguchia@psi.ch](mailto:zurab.guguchia@psi.ch)

order parameter realizing a higher angular momentum state, dubbed unconventional<sup>26,47–57</sup>, in analogy to superconducting orders. It is important to note that the charge order temperature in the above-mentioned kagome-lattice metals is limited to  $\approx 100$  K, and to the best of our knowledge, no order of charge order at room temperature exists so far.

A much less explored kagome lattice system is  $\text{LaRu}_3\text{Si}_2$ <sup>15–17,58–61</sup>. The structure of  $\text{LaRu}_3\text{Si}_2$  contains kagome layers of Ru sandwiched between layers of La and layers of Si having a honeycomb structure (see Fig. 1a)<sup>15,16</sup>. The superconductivity in  $\text{LaRu}_3\text{Si}_2$  is fully gapped<sup>17</sup> and has the highest SC transition temperature  $T_c \approx 7$  K among the kagome-lattice materials. Using first-principles calculations, we previously found that the normal state band structure features a kagome flat band, Dirac point, and Van Hove point formed by the Ru- $d_{z^2}$  orbitals near the Fermi level (see Fig. 1b). The electron-phonon coupling induced critical temperature  $T_c$ , estimated from the phonon dispersion<sup>17</sup>, was found to be much smaller than the experimental value. Thus, the enhancement of  $T_c$  in  $\text{LaRu}_3\text{Si}_2$  was attributed to the presence of the flat band, and the van Hove point relatively close to the Fermi level as well as to the high density of states from the narrow kagome bands<sup>17</sup>. Regarding the normal state properties, there is no report on either magnetic order or charge order in this system. Anomalous properties<sup>58,60</sup> in the normal state were inferred from thermodynamic measurements in  $\text{LaRu}_3\text{Si}_2$ , such as the deviation of the normal state-specific heat from the Debye model, non-mean field like suppression of superconductivity with magnetic field, and non-linear field dependence of the induced quasiparticle density of states (DOS). Previous studies have identified two potential structures for  $\text{LaRu}_3\text{Si}_2$  at room temperature: the  $P6/mmm$  (space group No. 191) and  $P6_3/m$  (space group No. 176). Our phonon dispersion calculations for both suggest that the  $P6/mmm$  structure is inherently unstable. This is evidenced by the appearance of three imaginary phonon modes in the  $k_z = \pi$  plane (see Fig. 1c), particularly at the A  $(0, 0, \frac{1}{2})$  point, indicating a propensity for this structure to transition into an  $a \times a \times 2c$  configuration, akin to the  $P6_3/m$  structure, to resolve this instability. Upon undergoing the  $a \times a \times 2c$  transformation, the phonon dispersion for the  $P6_3/m$  structure still displays two negative modes (see Fig. 1d), now relocated to the  $k_z = 0$  plane. One of these modes exhibits a flat dispersion within the  $k_z = 0$  plane, suggesting that the  $P6_3/m$  structure, while more stable than the  $P6/mmm$ , may still be prone to in-

plane structural reconstruction to reach a state of greater stability. These soft dispersions<sup>20–25</sup> signal the potential for charge-order phenomena, although the exact nature of the most stable in-plane reconstruction remains undetermined by density functional perturbation theory (DFPT) calculations alone.

In order to explore the possibility of a structural phase transition and the formation of charge order, we investigated three microcrystalline samples of  $\text{La}(\text{Ru}_{1-x}\text{Fe}_x)_3\text{Si}_2$  ( $x = 0, 0.01, 0.05$ ) as well as a large single crystal of  $\text{LaRu}_3\text{Si}_2$  via X-ray diffraction (the experimental details of which may be found in the methods section). The experiments reveal charge order with a propagation vector of  $(\frac{1}{3}, 0, 0)$  in undoped  $\text{LaRu}_3\text{Si}_2$  as well as Fe-doped  $\text{La}(\text{Ru}_{1-x}\text{Fe}_x)_3\text{Si}_2$  samples with  $x = 0.01$  and  $x = 0.05$ , setting in well above room temperature ( $T_{\text{CO,I}} \approx 400$  K). The charge order transition is preceded by a structural phase transition with  $T_{\text{str}} \approx 600$  K from the high-temperature hexagonal  $P6/mmm$  phase (space group (SG) No. 191) to the low-temperature orthorhombic  $Cccm$  phase (SG No. 66). Furthermore, a second set of charge order peaks with a propagation vector of  $(\frac{1}{6}, 0, 0)$  sets in below  $T_{\text{CO,II}} \approx 180$  K in the  $x = 0.01$  sample and possibly in the  $x = 0$  sample below  $T_{\text{CO,II}} \approx 80$  K, showing competition with the primary charge order.

## Results

Previous reports for both pristine and doped  $\text{LaRu}_3\text{Si}_2$ <sup>15,59,62,63</sup> have some discrepancy regarding the room temperature structure, represented either by a small hexagonal cell ( $P6/mmm$ ,  $a \approx 5.6$  Å,  $c \approx 3.5$  Å) (see Supplementary Note 1 and Supplementary Fig. 1) or a large hexagonal cell ( $P6_3/m$ ,  $a \approx 5.6$  Å,  $c \approx 7.1$  Å) (see Supplementary Fig. 2). Above 600 K, we found, from our single crystal diffraction experiments, that the crystal structure can indeed be described using a small hexagonal cell ( $P6/mmm$ ,  $a \times a \times c$ , HT-hex) (see Supplementary Fig. 1). The results of the refinement are summarized in the Supplementary Tables 1–5 (CCDC deposition number is 2289106). Attempts to introduce Fe in the Ru position for the  $x = 0.01$  Fe-doped sample yield 1.6(1)%, which agrees with the nominal value of 1% Fe-doping. Another peculiar feature is the presence of 5.6(2)% vacancies in the Si position.

Although the high-temperature model described above fits the diffraction data well, it features oblate thermal ellipsoids for Ru and Si atoms

**Fig. 1 | High-temperature crystal structure, band structure and phase diagram.** **a** Top view of the atomic structure of  $\text{LaRu}_3\text{Si}_2$ . The Ru atoms construct a kagome lattice (middle-size circles), while the Si (small-size circles) and La atoms (large-size circles) form a honeycomb and triangular structure, respectively. Structures were plotted using the VESTA visualization tool<sup>63</sup>. **b** The band structure (black) and orbital-projected band structure (red) for the Ru- $d_{z^2}$  orbital without spin-orbit coupling along the high symmetry  $k$ -path, presented in conformal kagome Brillouin zone (BZ). Calculation was done for the  $P6_3/m$  structure. The width of the line indicates the weight of each component. The blue-colored region highlights the manifestation of the kagome flat band. Arrows mark Dirac point (DP) and van Hove singularity point (VHS) formed by the Ru- $d_{z^2}$  orbitals near the Fermi level. **c** The phonon dispersion in the bulk of  $\text{LaRu}_3\text{Si}_2$  is characterized by the  $P6/mmm$  structure through the local density approximation. **d** The phonon dispersion in the bulk of  $\text{LaRu}_3\text{Si}_2$  is characterized by the  $P6_3/m$  structure through the local density approximation. The green-colored regions in panels **c** and **d** highlight the presence of imaginary phonon modes, one of which exhibits a flat dispersion.

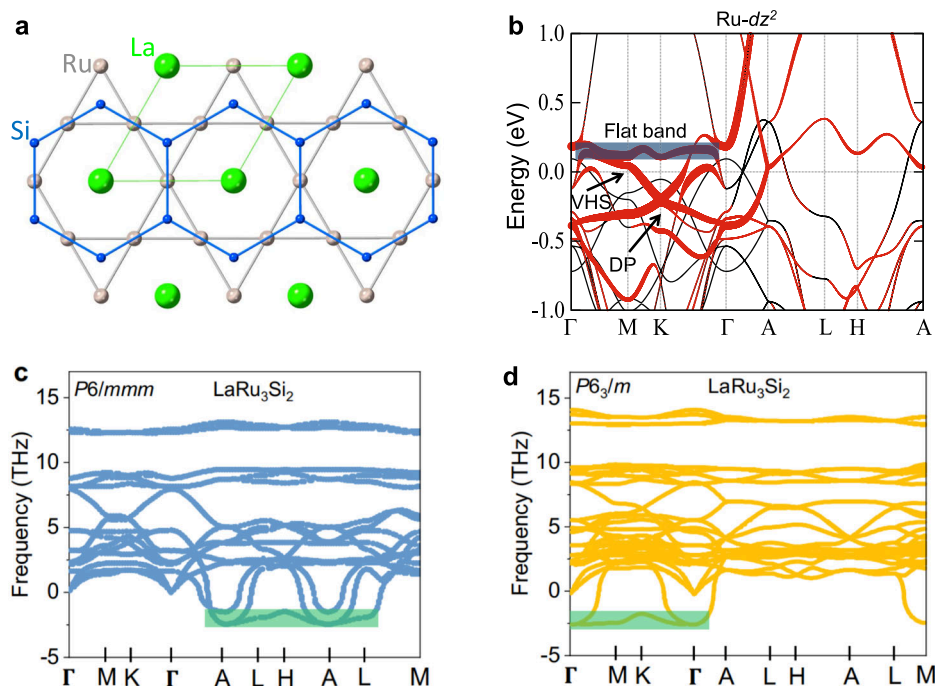


**Fig. 2 | Cascade of charge orders in**

**La(Ru<sub>1-x</sub>Fe<sub>x</sub>)<sub>3</sub>Si<sub>2</sub>.** Reconstructed reciprocal space along the (0 0 1) direction at 3 r.l.u. (reciprocal lattice units), performed at various temperatures for undoped a–e, as well as Fe-doped samples with  $x = 0.01$  f–j, and  $x = 0.05$  k–o. Arrows indicate the reciprocal space vectors. Orange, green, and blue circles mark the Bragg peak, primary charge order CO-I peak, and secondary charge order CO-II peak, respectively.

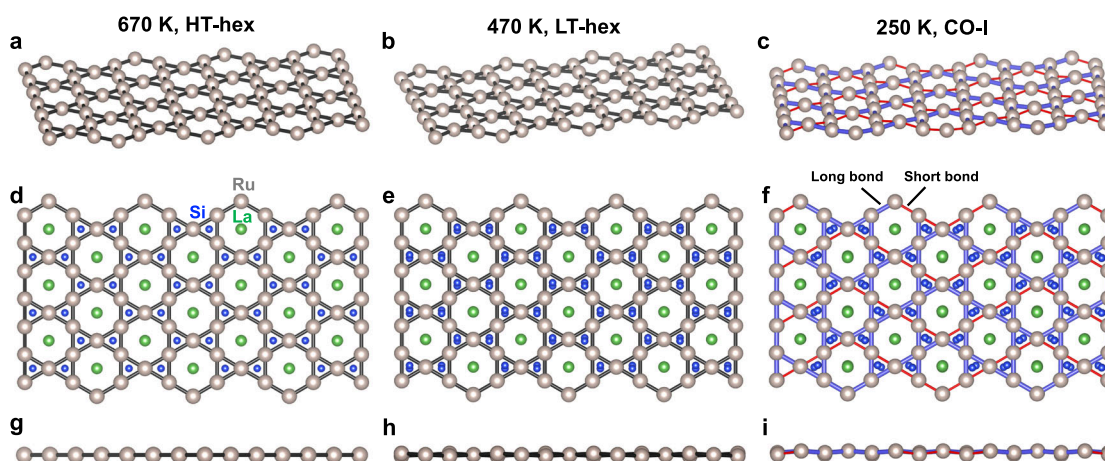
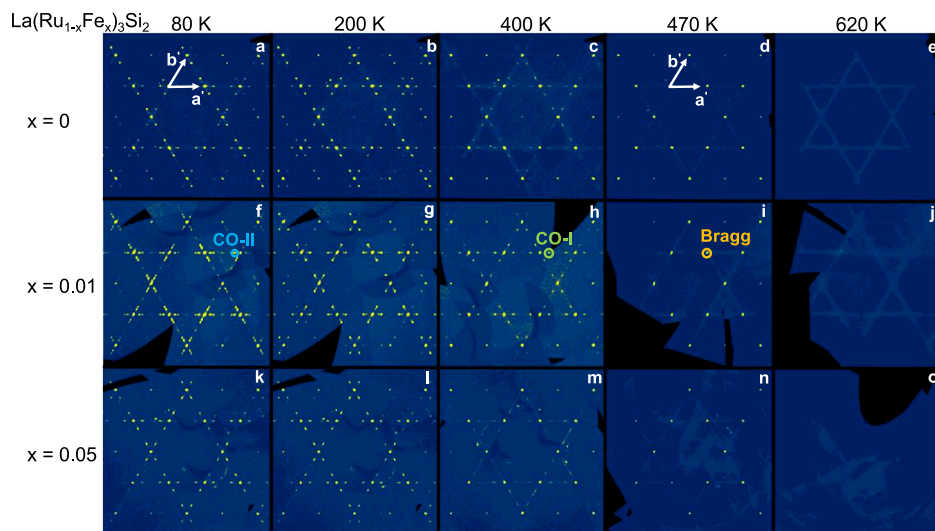


**Fig. 3 | Quantitative insight into various phases.** General projection of the kagome net at 670 K (HT-hex) (a), 470 K (LT-hex) (b), and 250 K (CO-I) (c), projection perpendicular to the kagome net at 670 K (d), 470 K (e), and 250 K (f), projection

along the kagome net at 670 K (g), 470 K (h) and 250 K (i). In panels c, f, i, the distances shorter than 2.845 Å are categorized as short and illustrated with a red line. The distances >2.845 Å are categorized as long and illustrated with a blue line.

(Supplementary Table 5). This, together with pronounced diffuse scattering within the  $(0, 0, l = \text{odd})$  reciprocal space planes (see Fig. 2d, e, I, j, n), indicates the proximity to a phase transition. Indeed, upon cooling below 600 K, we observe evolving Bragg peaks corresponding to the doubling of the initial unit cell along the  $c$ -axis ( $a \times a \times 2c$ , LT-hex), indicative of a structural phase transition (see also Supplementary Note 2 and Supplementary Fig. 5). The diffraction pattern follows hexagonal symmetry ( $R_{\text{int}} = 1.24\%$  for  $P6/mmm$  Laue symmetry) in agreement with the  $P6_3/m$  space group (SG No. 176), previously inferred from powder data<sup>15</sup>. Attempts to solve the crystal structure in this space group or any other down to  $P1$  are unsuccessful, which is likely an indication of twinning upon the structural phase transition. The structure can be described in the space group  $Cccm$  (No. 66) as three interpenetrating orthorhombic twins ( $a \times \sqrt{3}a \times 2c$ ) propagated by the six-fold axis present in the parent high-temperature phase. The refined twin fractions are close to  $\frac{1}{3}$ , which effectively mimics the six-fold symmetry of the diffraction pattern.

Below  $\sim 400$  K, the diffuse scattering is clustered into another set of sharp diffraction spots. Besides the main reflections, there are satellites corresponding to  $q_1 = (\frac{1}{4} 0 0)$ ,  $q_2 = (0 \frac{1}{4} 0)$  and  $q_3 = (\frac{1}{4} \frac{-1}{4} 0)$  relative to the  $a \times a \times 2c$  cell (see Fig. 2c–e, Supplementary note 1 and Supplementary Fig. 4); the refined deviations from the rational fractions are within  $3\sigma$ . The diffraction pattern thus represents a  $4 \times 4 \times 1$  superstructure (see

Supplementary Fig. 3) of the parent diffraction pattern existing above  $\sim 400$  K; all reflections can be indexed using a  $4a \times 4a \times 2c$  supercell. Similar to the case of LT-hex, the structure can be solved in this supercell in an orthorhombic unit cell ( $Cccm$ , 40 symmetrically independent atoms), assuming twinning by the six-fold axis. The disadvantage of this description is that it also accounts for higher-order satellite peaks besides  $q_1, q_2$ , and  $q_3$ , including cross-satellites ( $2q_1, q_1q_2$ , etc.), which are practically unobservable. This hints at the possibility of describing the CO-I phase with a smaller cell. Indeed, the initial supercell can be reduced to  $a \times 2\sqrt{3}a \times 2c$  or  $a \times \sqrt{3}a \times 2c$  with  $q = (0 \frac{1}{2} 0)$  cell without losing observable reflections. Here,  $q = (0 \frac{1}{2} 0)$  corresponds to a high symmetry direction (DT line) in the Brillouin zone. Within this cell, the structure can be described as modulated in superspace group  $Cmmm(0b0)s00$ . Superlattice peak intensity appears below  $T_{\text{CO,I}} \simeq 400$  K for undoped  $\text{LaRu}_3\text{Si}_2$  (Fig. 2a–e) as well as Fe-doped  $\text{La}(\text{Ru}_{1-x}\text{Fe}_x)_3\text{Si}_2$  samples with  $x = 0.01$  and  $x = 0.05$  as shown in Fig. 2a–e, f–j, and k–o, respectively. The charge order features for the  $x = 0.05$  sample look broader, as compared to  $x = 0$  and  $0.01$  samples, and do not coalesce into sharp diffraction peaks right below  $\simeq 400$  K. This indicates that the effect of Fe-doping is to introduce disorder into the charge order. Another set of reflections evolves at positions corresponding to  $q'_1 = (\frac{1}{6} 0 0)$ ,  $q'_2 = (0 \frac{1}{6} 0)$  and  $q'_3 = (\frac{1}{6} \frac{-1}{6} 0)$ , which is most pronounced for the  $x = 0.01$  sample with  $T_{\text{CO,II}} \simeq 180$  K.

Since the relation between these two sets of ordering vectors is unclear (multi-phase vs. multi- $q$  ordering) we refrain from speculating on the possible models of superstructure ordering.

Comparison of models for HT-hex (at 670 K), LT-hex (at 470 K) and CO-I (at 250 K) phases is provided in Fig. 3a–i. The HT-hex phase features an undistorted planar kagome net comprised of Ru atoms alternating with Si/La planes (Fig. 3a,d,g). The distances within the Ru-kagome net are 2.844(4) Å. Alternatively, this structure can be viewed as packing of La polyhedra comprised of 6 Si atoms ( $d(\text{La-Si}) = 3.284(5)$  Å) and 12 Ru atoms ( $d(\text{La-Ru}) = 3.357(3)$  Å) reinforced by short Si–Ru contacts ( $d(\text{Si-Ru}) = 2.424(6)$  Å). The transition to the LT-hex phase is mainly due to in-plane displacement of Si atoms, distortion of the environment of La, and very small out-of-plane displacements of 2/3 of Ru atoms (Fig. 3b, e, h). In particular, this leads to very weak corrugations of the ideal kagome net with shortening and elongation of Ru–Ru distances ( $4 \times 2.8431(7)$  Å +  $2 \times 2.853(1)$  Å), still retaining a nearly ideal hexagonal Ru-plane. Upon further cooling and transition into the CO-I phase, there occurs a strong disproportionation of bonds, resulting in the emergence of short and long Ru–Ru bonds, which is to say, a bond or charge order is established. The Ru–Ru distances are in the range of 2.832(1)–2.868(1) Å. In Fig. 3c, f, i, the distances below 2.845 Å are marked as short, and the distances above 2.845 Å are marked as long. So, our comprehensive analysis shows that the structural phase transition at  $T_{\text{str}} \simeq 600$  K leads to a minimal distortion of the Ru kagome plane, thereby preserving a nearly ideal kagome lattice structure, and charge order is established only below  $T_{\text{CO,I}} \simeq 400$  K. Charge ordering results from the ordering of Ru–Ru bonds, a phenomenon of particular interest due to the Ru- $d_{z^2}$  orbital's formation of a distinctive kagome band structure, suggesting a potential link between charge ordering and the underlying physics of the kagome lattice.

Figure 4a and b outline four distinct temperature regions for  $\text{La}(\text{Ru}_{1-x}\text{Fe}_x)_3\text{Si}_2$  by following selected main and supposedly superstructure reflections. Namely, Fig. 4a and b show the temperature dependences of the intensities of the (2 –3 5) (hexagonal setting) Bragg peak and the charge-order peak intensities, respectively, for  $x = 0, 0.01$ , and  $0.05$  samples. By tracking the relative intensity of CO-I and CO-II peaks for the different doped samples, we find that in the  $x = 0.01$  case, there is a clear decrease in the scattered intensity from the CO-I phase at the same temperature where the scattered intensity from the CO-II phase appears. The intensity of the peaks from the CO-II phase increases while the intensity of the peaks from the CO-I monotonously decreases until they achieve equivalent intensities at 80 K. This implies that the two charge-ordered phases compete. We note that the onset of this additional modulated structure CO-II appears to be enhanced in the  $x = 0.01$  Fe-doped sample, occurring at 180 K, while weak peaks become visible below 120–100 K in the pristine sample. The intensity of the CO-I phase seems to reach a peak at 120 K and decrease from 120 to 80 K in the undoped material, suggesting that the onset of the CO-II phase may be at lower temperatures. No signatures of coherent or diffuse scattering at  $\frac{1}{6}$  periodicity are observed in the  $x = 0.05$  Fe-doped sample, which is most likely due to disorder-induced broadening of the charge order peaks. The intensities of the (2 –3 5) (hexagonal setting) Bragg peak for  $x = 0, 0.01$ , and  $0.05$  samples (see Fig. 4a) show a clear slope change around  $T_{\text{CO,I}} \simeq 400$  K and an additional slope change with an increase in (2 –3 5) intensity below  $T_{\text{CO,II}} \simeq 180$  K for all three samples. Increase of Bragg peak intensity across  $T_{\text{CO,II}}$  is most pronounced in the  $x = 0.01$  sample in which a clear indication of  $\frac{1}{6}$  charge order is observed. Figure 5 presents a phase diagram summarizing the charge order and superconducting transition temperatures for  $\text{La}(\text{Ru}_{1-x}\text{Fe}_x)_3\text{Si}_2$ . This diagram indicates that the onset of the CO-I phase remains constant despite Fe doping, although the superconducting transition temperature  $T_c$  is strongly suppressed. However, the effects on the CO-II phase and its interaction with superconductivity are not yet clear, indicating the need for further low-temperature experimental investigations.

## Discussion

Before concluding, we clarify our use of the term ‘charge order’, initially defined to describe Peierls-type instabilities<sup>64</sup> characterized by periodic

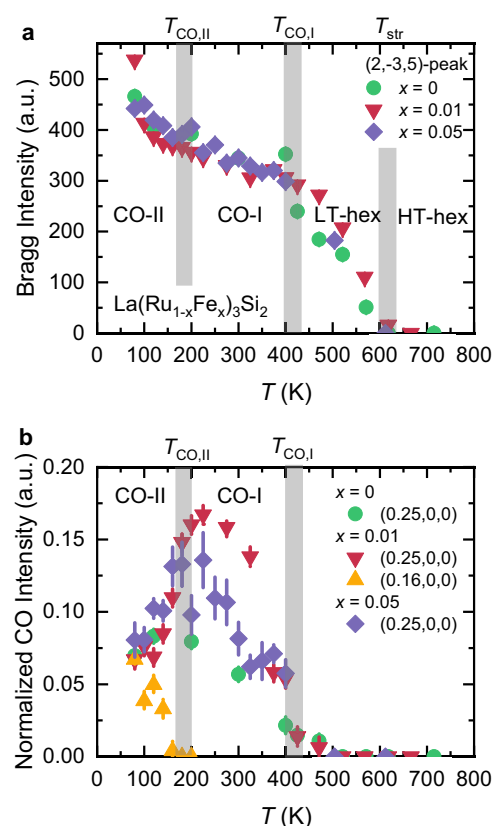


**Fig. 4 | Structural phases and charge orders in  $\text{La}(\text{Ru}_{1-x}\text{Fe}_x)_3\text{Si}_2$ .** Temperature evolution of the Bragg intensity (a) and charge order satellite peak intensities (b). The error bars represent the standard deviation of the fit parameters.

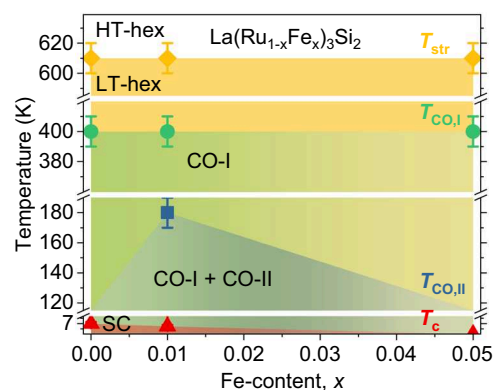


**Fig. 5 | Phase diagram of  $\text{La}(\text{Ru}_{1-x}\text{Fe}_x)_3\text{Si}_2$ .** The Fe-doping evolution of the superconducting transition temperature  $T_c$  (data are taken from our previous work ref. 61), charge order transition temperatures  $T_{\text{CO,I}}$ ,  $T_{\text{CO,II}}$  and structural phase transition temperature  $T_{\text{str}}$ . The plots include error bars that indicate the standard error. The standard error is a measure of the variability or precision of a sample mean.

charge density fluctuations without changes in atomic positions. It was shown<sup>65</sup> that original Peierls construction about purely electronically driven charge order is unlikely to apply to real materials. Even in prototypical charge-ordered materials like  $\text{NbSe}_2$ <sup>66,67</sup>,  $\text{TaSe}_2$ ,  $\text{TiSe}_2$ <sup>68</sup>, and  $\text{CeTe}_3$ , Peierls conditions are hardly fulfilled. Instead, charge order transitions were shown to be driven by the concerted action of electronic and ionic subsystems, i.e., a momentum-dependent electron–phonon coupling plays an essential part (provided that the electronic degrees of freedom enhance the electron–phonon matrix elements). Giant electron–phonon coupling

associated with charge order was also observed in copper oxide superconductors<sup>69</sup>. In summary, charge order in crucial materials like cuprates and TMDs seems to be the result of synergy between electronic and ionic subsystems. This synergy is likely present in the LaRu<sub>3</sub>Si<sub>2</sub> and other kagome metals as well<sup>22,23,36,48,70</sup>. In accordance with more recent literature, such as on AV<sub>3</sub>Sb<sub>5</sub>, ScV<sub>6</sub>Sn<sub>6</sub>, and FeGe, we use the term ‘charge order’ to encompass a variety of phenomena, including both electronic and atomic modulations with incommensurate or extended periodicity. Specifically, we apply this term to denote the static and long-range Ru–Ru bond order observed in La(Ru<sub>1-x</sub>Fe<sub>x</sub>)<sub>3</sub>Si<sub>2</sub>. Our study does not imply a purely electronic origin of this order<sup>65</sup> since, in actual materials, the formation of charge density waves is a complex process involving both lattice distortions and electronic instabilities.

Experimental realizations of charge order in the kagome lattice have long been awaited. It was not until recently when studies into the family of kagome metals AV<sub>3</sub>Sb<sub>5</sub> (A = K, Rb, Cs)<sup>9,18,19,29–31</sup>, ScV<sub>6</sub>Sn<sub>6</sub><sup>20,21</sup> and magnetic FeGe<sup>36–28</sup> revealed charge-ordered states. However, the charge-ordering temperature in all these materials is limited to  $\approx 100$  K, i.e., well below room temperature. Also, among the above-mentioned systems it is only the AV<sub>3</sub>Sb<sub>5</sub> family of materials that shows superconductivity. In these systems, charge order strongly competes with superconductivity and has a negative effect on both the superconducting critical temperature and the superfluid density. Therefore, the maximum SC transition temperature, in the presence of charge order, was reported to be  $\approx 3$  K. Here, we report the discovery of the cascade of charge orders in La(Ru<sub>1-x</sub>Fe<sub>x</sub>)<sub>3</sub>Si<sub>2</sub> ( $x = 0–0.05$ ): the one with a propagation vector of  $(\frac{1}{4}, 0, 0)$ , setting in well above room temperature ( $T_{COI} \approx 400$  K) and a second one with a propagation vector of  $(\frac{1}{6}, 0, 0)$ , setting in at lower temperatures, which competes with the primary charge order. Moreover, the system LaRu<sub>3</sub>Si<sub>2</sub> exhibits the highest superconducting critical temperature  $T_c \approx 7$  K and the highest superfluid density<sup>17</sup> among the known bulk kagome-lattice superconductors. This implies that in this system, both charge order and superconductivity are somewhat optimized, irrespective of the mechanism involved. Fe-doping does introduce significant disorder to the charge-ordered state and leads to the full suppression of superconductivity with  $x_{Fe,cr} = 0.05$ <sup>61</sup>. Our results classify the bulk superconductor LaRu<sub>3</sub>Si<sub>2</sub> as the kagome-lattice system with charge order above room temperature. This finding, combined with the three-dimensional character of superconductivity, unlike the mainly two-dimensional properties of AV<sub>3</sub>Sb<sub>5</sub>, positions LaRu<sub>3</sub>Si<sub>2</sub> as an outstanding model to study the inherent mechanisms and to analyze the relationship between charge order and superconductivity. Moreover, to the best of our knowledge the system LaRu<sub>3</sub>Si<sub>2</sub> has the highest long-range charge-order temperature among the superconducting materials. The importance of this discovery of above room temperature charge order is not limited to kagome lattice materials, and we anticipate will have a broader impact. Previous research in quantum materials has unearthed complex interactions between charge order and electronic phases, including direct competition with superconductivity or mediation of colossal magnetoresistance, which highlights the importance of charge order in understanding these novel phases of matter. It's also noteworthy that the series of phase transitions observed in LaRu<sub>3</sub>Si<sub>2</sub> bear a resemblance to those in cuprates, like the La<sub>2-x</sub>Ba<sub>x</sub>CuO<sub>4</sub><sup>1</sup> system with  $x = 1/8$ , and in TMDs<sup>67</sup>. These phenomena encompass structural phase transitions, charge ordering, and superconductivity. However, unlike the cuprates where charge order manifests as stripe order, LaRu<sub>3</sub>Si<sub>2</sub> exhibits charge ordering in the form of bond order, similar to patterns observed in other Kagome systems and certain TMDs, such as IrTe<sub>2</sub><sup>67</sup>. The comparison of LaRu<sub>3</sub>Si<sub>2</sub> with cuprates and TMDs becomes particularly fascinating, given the higher charge order transition temperatures in LaRu<sub>3</sub>Si<sub>2</sub>.

Besides the fundamental aspect, room-temperature charge order may be useful in charge order-based electronic devices<sup>71,72</sup>. Switching between various material phases near room temperature is a promising step toward next-generation electronic and optoelectronic technologies. There is an example of an oscillator based on an integrated TaS<sub>2</sub>–boron nitride–graphene device, which utilizes the charge order phase transition<sup>71</sup>.

Previous works have also discussed the implementation of charge order transition-based devices<sup>72</sup> for information processing and radiation-hard applications. In theory, such devices can be fast, low-power, and immune to proton and X-ray radiation. Also, the quasi-two-dimensional structure of LaRu<sub>3</sub>Si<sub>2</sub> naturally leads to the question of whether thin layers or even monolayers can be exfoliated. Thin films would allow the formation of Moire structures by gating, stacking, or twisting, promising exciting future developments. This could also facilitate the further exploration of superconducting and charge-ordered phases.

Having established the existence of high-temperature charge order in the kagome material LaRu<sub>3</sub>Si<sub>2</sub>, our study opens up exciting avenues for future quantum materials research. In the kagome compounds, ScV<sub>6</sub>Sn<sub>6</sub><sup>20–22,25</sup> and AV<sub>3</sub>Sb<sub>5</sub> (A = K, Rb, Cs)<sup>29,32,33,44,47,49,73–75</sup>, the interplay of electronic and phononic contributions in the formation of charge order have been at the heart of the scientific discourse. It seems clear that both the low-energy fermiology as well as the phononic instabilities have to be considered to explain the charge order with its unconventional properties, such as chiral charge order that can be sensitively manipulated by strain and magnetic fields. While charge order in this context means a translation symmetry breaking instability ( $Q \neq 0$  order), there exists the equally relevant possibility of an intra-unit cell ( $Q = 0$ ) charge order in which low energy electronic states are involved. The loop current phases of the Haldane honeycomb model<sup>76</sup> or the Varma model<sup>77</sup> for the cuprate superconductors are prominent examples. Following this line of thought blurs the boundaries between structural transitions and charge orders. It is thus imperative to study the electronic response and electronic structure of LaRu<sub>3</sub>Si<sub>2</sub> in more detail to unveil its connections with the changes in structural motifs found in this work.

## Methods

### Sample preparation

The samples of La(Ru<sub>1-x</sub>Fe<sub>x</sub>)<sub>3</sub>Si<sub>2</sub> were synthesized from high-purity Si lump (purity 99.999+%, Alpha aesar), low-oxygen vacuum remelted Fe lump (purity 99.99%, Alpha aesar), Ru pellets (purity 99.95%, Alpha aesar), and La ingot (purity 99.9%) via arc melting using Zr pellets as an oxygen getter. The melted buttons were flipped three times to ensure melt homogenization. In order to suppress the second phase LaRu<sub>2</sub>Si<sub>2</sub>, an additional 15% Ru was added to each melt (as mentioned previously<sup>59,62,63</sup>) in order to attain nominal compositions as La(Ru<sub>1-x</sub>Fe<sub>x</sub>)<sub>3.45</sub>Si<sub>2</sub>. Single crystals of La(Ru<sub>1-x</sub>Fe<sub>x</sub>)<sub>3</sub>Si<sub>2</sub> were extracted from arc-melted buttons.

Polycrystalline sample of LaRu<sub>3</sub>Si<sub>2</sub> was prepared by arc-melting mixtures of lanthanum, ruthenium and silicon in a purified argon atmosphere. The polycrystalline materials with excess Ru obtained were used to grow single crystal of LaRu<sub>3</sub>Si<sub>2</sub> by the Czochralski method, using a commercial tetra-arc furnace (TAC-5100, GES). Our X-ray measurements indicate a single phase of hexagonal LaRu<sub>3</sub>Si<sub>2</sub> phase.

### Single crystal diffraction measurements

Single crystalline samples were selected from the large undoped crystal and from crushed chunks of the arc-melted samples washed in dilute HCl for 5 min before being flushed in deionized H<sub>2</sub>O and ethanol, followed by acetone to dry them. Following this, we selected single crystalline samples that had faceted sides and a typical size of 30–100  $\mu$ m. These were then mounted on a small-diameter (10  $\mu$ m) MiTeGen loop or a quartz capillary and centered within the X-ray beam. Diffraction measurements were carried out using the laboratory STOE STADIVARI single crystal diffractometer at the Paul Scherrer Institute. Measurements were carried out in the temperature range between 80 and 700 K, using the combination of the CryoStream (constant N<sub>2</sub> gas flow) and HeatStream (constant Ar flow of 0.8 L/min). The micro-focused source was a Mo K $\alpha$  X-ray with a wavelength of 0.71073 Å. The detector was a Dectris EIGER 1M 2R. The exposure time was set to 10 s per frame, and the coverage was calculated through the program X-Area<sup>78</sup>. Data reduction and correction were done with the X-Area package. The peaks were identified by the X-Area software (typically taking a minimum Intensity/ $\sigma \geq 25$ ), and then the lattice parameters were

refined. From this, we were able to integrate the intensities and extract individual Bragg peak and CO peak intensities for each  $q$ -vector (modulation). These intensities were corrected by beam-out and frame scaling and then further by spherical correction (where the absorption  $\mu$  and sample radius were inputs). From this, we were able to identify the strongest CO satellite intensities and follow them with temperature. We also used the X-Area software to perform reconstructions in the reciprocal space of the collected data (see Fig. 2) in order to visually identify changes in the charge order periodicity and structure. We used the software JANA2020 for data refinement and  $\mu$  calculation<sup>79</sup>. The large single crystal of LaRu<sub>3</sub>Si<sub>2</sub> was also measured at room temperature in the hard X-ray beamline (P21.1, PETRA III) at the DESY facility, and the superlattice peaks due to charge order were identified.

### Density functional perturbation theory

Density functional perturbation theory (DFPT) method is based on the harmonic approximation of phonons, which inherently does not account for temperature variations<sup>80</sup>. Consequently, DFPT is unable to directly predict temperature-dependent properties. The observed negative phonon energy in our results just suggests a potential for structural instability rather than predicting a specific temperature for a structural phase transition. To accurately determine the temperature at which such transition may occur, alternative methods like the temperature-dependent effective potential method<sup>81</sup> or the more recent stochastic self-consistent harmonic approximation method<sup>82</sup>, are more suitable. These approaches are of great interest for future studies, potentially providing a deeper understanding of the temperature-dependent dynamics of structural phase transitions.

### Data availability

All relevant data are available from the corresponding authors.

Received: 19 April 2024; Accepted: 22 May 2024;

Published online: 08 June 2024

### References

- Tranquada, J. M., Sternlieb, B. J., Axe, J. D., Nakamura, Y. & Uchida, S. Evidence for stripe correlations of spins and holes in copper oxide superconductors. *Nature* **375**, 561–563 (1995).
- Chang, J. et al. Direct observation of competition between superconductivity and charge density wave order in YBa<sub>2</sub>Cu<sub>3</sub>O<sub>6.67</sub>. *Nat. Phys.* **8**, 871–876 (2012).
- Da Silva Neto, E. H. et al. Charge ordering in the electron-doped superconductor Nd<sub>2-x</sub>Ce<sub>x</sub>CuO<sub>4</sub>. *Science* **347**, 282–285 (2015).
- Atfield, J. P. Charge ordering in transition metal oxides. *Solid State Sci.* **8**, 861–867 (2006).
- Johannes, M. D., Mazin, I. I. & Howells, C. A. Fermi-surface nesting and the origin of the charge-density wave in NbSe<sub>2</sub>. *Phys. Rev. B* **73**, 205102 (2006).
- Yu, R. et al. Phase separation at the dimer-superconductor transition in Ir<sub>1-x</sub>Rh<sub>x</sub>Te<sub>2</sub>. *Phys. Rev. B* **98**, 134506 (2018).
- Ivashko, O. et al. Charge-stripe order and superconductivity in Ir<sub>1-x</sub>Pt<sub>x</sub>Te<sub>2</sub>. *Sci. Rep.* **7**, 17157 (2017).
- Guguchia, Z., Khasanov, R. & Luetkens, H. Unconventional charge order and superconductivity in kagome-lattice systems as seen by muon-spin rotation. *npj Quantum Mater.* **8**, 41 (2023).
- Ortiz, B. et al. CsV<sub>3</sub>Sb<sub>5</sub>: a Z<sub>2</sub> topological kagome metal with a superconducting ground state. *Phys. Rev. Lett.* **125**, 247002 (2020).
- Syozji, I. Statistics of kagome lattice. *Prog. Theor. Phys.* **6**, 306 (1951).
- Yin, J.-X., Lian, B. & Hasan, M. Z. Topological kagome magnets and superconductors. *Nature* **612**, 647–657 (2022).
- Ye, L. Massive Dirac fermions in a ferromagnetic kagome metal. *Nature* **555**, 638–642 (2018).
- Ghimire, N. J. & Mazin, I. I. Topology and correlations on the kagome lattice. *Nat. Mater.* **19**, 137–138 (2020).
- Guguchia, Z. et al. Tunable anomalous Hall conductivity through volume-wise magnetic competition in a topological kagome magnet. *Nat. Commun.* **11**, 559 (2020).
- Barz, H. Ternary transition metal phosphides: High-temperature superconductors. *Mater. Res. Bull. PNAS* **15**, 1489 (1980).
- Vandenberg, J.M., Barz, H. Ternary transition metal phosphides: High-temperature superconductors. *Mater. Res. Bull. PNAS* **15**, 1493 (1980).
- Mielke III, C. et al. Nodeless kagome superconductivity in LaRu<sub>3</sub>Si<sub>2</sub>. *Phys. Rev. Mater.* **5**, 034803 (2021).
- Ortiz, B. et al. Superconductivity in the Z<sub>2</sub> kagome metal KV<sub>3</sub>Sb<sub>5</sub>. *Phys. Rev. Mater.* **5**, 034801 (2021).
- Yin, Q. et al. Superconductivity and normal-state properties of kagome metal RbV<sub>3</sub>Sb<sub>5</sub> single crystals. *Chinese Phys. Lett.* **38**, 037403 (2021).
- Suriya Arachchige, H. W. et al. Charge density wave in kagome lattice intermetallic ScV<sub>6</sub>Sn<sub>6</sub>. *Phys. Rev. Lett.* **129**, 216402 (2022).
- Guguchia, Z. Hidden magnetism uncovered in charge ordered bilayer kagome material ScV<sub>6</sub>Sn<sub>6</sub>. *Nat. Commun.* **14**, 7796 (2023).
- Hu, H. et al. Kagome materials I: SG 191, ScV<sub>6</sub>Sn<sub>6</sub>. Flat phonon soft modes and unconventional CDW formation: microscopic and effective theory. arXiv:2305.15469 (2023).
- Korshunov, A. Softening of a flat phonon mode in the kagome ScV<sub>6</sub>Sn<sub>6</sub>. *Nat. Commun.* **14**, 6646 (2023).
- Cao, S. Competing charge-density wave instabilities in the kagome metal ScV<sub>6</sub>Sn<sub>6</sub>. *Nat. Commun.* **14**, 7671 (2023).
- Hu, Y. et al. Phonon promoted charge density wave in topological kagome metal ScV<sub>6</sub>Sn<sub>6</sub>. *Nat. Commun.* **15**, 1658 (2024).
- Teng, X. Discovery of charge density wave in a kagome lattice antiferromagnet. *Nature* **609**, 490–495 (2022).
- Yin, J.-X. Discovery of charge order and corresponding edge state in kagome magnet FeGe. *Phys. Rev. Lett.* **129**, 166401 (2022).
- Teng, X. Magnetism and charge density wave order in kagome FeGe. *Nat. Phys.* **19**, 814–822 (2023).
- Jiang, Y.-X. et al. Discovery of topological charge order in kagome superconductor KV<sub>3</sub>Sb<sub>5</sub>. *Nat. Mater.* **20**, 1353–1357 (2021).
- Shumiya, N. et al. Tunable chiral charge order in kagome superconductor RbV<sub>3</sub>Sb<sub>5</sub>. *Phys. Rev. B* **104**, 035131 (2021).
- Wang, Z. et al. Electronic nature of chiral charge order in the kagome superconductor CsV<sub>3</sub>Sb<sub>5</sub>. *Phys. Rev. B* **104**, 075148 (2021).
- Mielke III, C. et al. Time-reversal symmetry-breaking charge order in a kagome superconductor. *Nature* **602**, 245–250 (2022).
- Guguchia, Z. et al. Tunable unconventional kagome superconductivity in charge ordered RbV<sub>3</sub>Sb<sub>5</sub> and KV<sub>3</sub>Sb<sub>5</sub>. *Nat. Commun.* **14**, 153 (2023).
- Khasanov, R. et al. Time-reversal symmetry broken by charge order in CsV<sub>3</sub>Sb<sub>5</sub>. *Phys. Rev. Res.* **4**, 023244 (2022).
- Yu, L. et al. Evidence of a hidden flux phase in the topological kagome metal CsV<sub>3</sub>Sb<sub>5</sub>. arXiv:2107.10714 (2021).
- Hu, Y. et al. Coexistence of tri-hexagonal and star-of-david pattern in the charge density wave of the kagome superconductor AV<sub>3</sub>Sb<sub>5</sub>. *Phys. Rev. B* **106**, L241106 (2022).
- Xu, Y. et al. Three-state nematicity and magneto-optical Kerr effect in the charge density waves in kagome superconductors. *Nat. Phys.* **18**, 1470–1475 (2022).
- Guo, C. et al. Switchable chiral transport in charge-ordered kagome metal CsV<sub>3</sub>Sb<sub>5</sub>. *Nature* **611**, 461–466 (2022).
- Wu, Q. et al. Simultaneous formation of two-fold rotation symmetry with charge order in the kagome superconductor CsV<sub>3</sub>Sb<sub>5</sub> by optical polarization rotation measurement. *Phys. Rev. B* **106**, 205109 (2022).
- Hu, Y. et al. Time-reversal symmetry breaking in charge density wave of CsV<sub>3</sub>Sb<sub>5</sub> detected by polar Kerr effect. Preprint at <https://doi.org/10.48550/arXiv.2208.08036> (2023).
- Li, H. et al. Rotation symmetry breaking in the normal state of a kagome superconductor KV<sub>3</sub>Sb<sub>5</sub>. *Nat. Phys.* **18**, 265–270 (2022).

42. Saykin, D. R. et al. High resolution polar Kerr effect studies of CsV<sub>3</sub>Sb<sub>5</sub>: tests for time reversal symmetry breaking below the charge order transition. *Phys. Rev. Lett.* **131**, 016901 (2023).
43. Xing, Y. et al. Optical manipulation of the charge density wave state in RbV<sub>3</sub>Sb<sub>5</sub>. arXiv:2308.04128 (2023).
44. Neupert, T., Denner, M. M., Yin, J.-X., Thomale, R. & Hasan, M. Z. Charge order and superconductivity in kagome materials. *Nat. Phys.* **18**, 137–143 (2022).
45. Yang, S. Giant, unconventional anomalous Hall effect in the metallic frustrated magnet candidate, KV<sub>3</sub>Sb<sub>5</sub>. *Sci. Adv.* **6**, 1–7s (2020).
46. Yu, F. Concurrence of anomalous Hall effect and charge density wave in a superconducting topological kagome metal. *Phys. Rev. B* **104**, 041103 (2021).
47. Denner, M., Thomale, R. & Neupert, T. Analysis of charge order in the kagome metal AV<sub>3</sub>Sb<sub>5</sub> (A = K, Rb, Cs). *Phys. Rev. Lett.* **127**, 217601 (2022).
48. Christensen, M. H., Birol, T., Andersen, B. M. & Fernandes, R. M. Theory of the charge-density wave in AV<sub>3</sub>Sb<sub>5</sub> kagome metals. *Phys. Rev. B* **104**, 214513 (2021).
49. Christensen, M. H., Birol, T., Andersen, B. M. & Fernandes, R. M. Loop currents in AV<sub>3</sub>Sb<sub>5</sub> kagome metals: multipolar and toroidal magnetic orders. *Phys. Rev. B* **106**, 144504 (2022).
50. Ritz, E. T., Fernandes, R. M. & Birol, T. Impact of Sb degrees of freedom on the charge density wave phase diagram of the kagome metal CsV<sub>3</sub>Sb<sub>5</sub>. *Phys. Rev. B* **107**, 205131 (2023).
51. Tazai, R., Yamakawa, Y., Onari, S. & Kontani, H. Mechanism of exotic density-wave and beyond-Migdal unconventional superconductivity in kagome metal AV<sub>3</sub>Sb<sub>5</sub> (A = K, Rb, Cs). *Sci. Adv.* **8**, eabl4108 (2022).
52. Park, T., Ye, M. & Balents, L. Electronic instabilities of kagome metals: saddle points and Landau theory. *Phys. Rev. B* **104**, 035142 (2021).
53. Lin, Y.-P. & Nandkishore, R. M. Complex charge density waves at Van Hove singularity on hexagonal lattices: haldane-model phase diagram and potential realization in the kagome metals AV<sub>3</sub>Sb<sub>5</sub>. *Phys. Rev. B* **104**, 045122 (2021).
54. Chandan Setty, C., Hu, H., Chen, L. & Si, Q. Electron correlations and T-breaking density wave order in a Z<sub>2</sub> kagome metal. Preprint at <https://arxiv.org/abs/2105.15204> (2021).
55. Song, D. et al. Orbital ordering and fluctuations in a kagome superconductor CsV<sub>3</sub>Sb<sub>5</sub>. *Sci. China Phys. Mech. Astron.* **65**, 247462 (2022).
56. Grandi, F. et al. Theory of nematic charge orders in kagome metals. *Phys. Rev. B* **107**, 155131 (2023).
57. Tazai, R., Yamakawa, Y. & Kontani, H. Drastic magnetic-field-induced chiral current order and emergent current-bond-field interplay in kagome metal AV<sub>3</sub>Sb<sub>5</sub> (A = Cs, Rb, K). *PNAS* **121**, e2303476121 (2023).
58. Kishimoto, Y. et al. Magnetic susceptibility study of LaRu<sub>3</sub>Si<sub>2</sub>. *J. Phys. Soc. Jpn.* **71**, 2035–2038 (2002).
59. Li, B., Li, S. & Wen, H.-H. Chemical doping effect in the LaRu<sub>3</sub>Si<sub>2</sub> superconductor with a kagome lattice. *Phys. Rev. B* **94**, 094523 (2016).
60. Li, S. Anomalous properties in the normal and superconducting states of LaRu<sub>3</sub>Si<sub>2</sub>. *Phys. Rev. B* **84**, 214527 (2011).
61. Mielke III, C. et al. Microscopic study of the impurity effect in the kagome superconductor La(Ru<sub>1-x</sub>Fe<sub>x</sub>)<sub>3</sub>Si<sub>2</sub>. *Phys. Rev. B* **109**, 134501 (2024).
62. Li, S. et al. Anomalous properties in the normal and superconducting states of LaRu<sub>3</sub>Si<sub>2</sub>. *Phys. Rev. B* **84**, 214527 (2011).
63. Li, S. et al. Distinct behaviors of suppression to superconductivity in LaRu<sub>3</sub>Si<sub>2</sub> induced by Fe and Co dopants. *Phys. Rev. B* **86**, 024513 (2012).
64. Peierls, R. E. *Quantum Theory of Solids* (Oxford University, London, 1955).
65. Johannes, M. D. & Mazin, I. I. Fermi surface nesting and the origin of charge density waves in metals. *Phys. Rev. B* **77**, 165135 (2008).
66. Flicker, F. & van Wezel, J. Charge order from orbital-dependent coupling evidenced by NbSe<sub>2</sub>. *Nat. Commun.* **6**, 7034 (2015).
67. Weber, F. et al. Extended phonon collapse and the origin of the charge-density wave in 2H-NbSe<sub>2</sub>. *Phys. Rev. Lett.* **107**, 107403 (2011).
68. Weber, F. et al. Electron-phonon coupling and the soft phonon mode in TiSe<sub>2</sub>. *Phys. Rev. Lett.* **107**, 266401 (2011).
69. Reznik, D. et al. Electron-phonon coupling reflecting dynamic charge inhomogeneity in copper oxide superconductors. *Nature* **440**, 1170–1173 (2006).
70. Luo, H. et al. Electronic nature of charge density wave and electron-phonon coupling in kagome superconductor KV<sub>3</sub>Sb<sub>5</sub>. *Nat. Commun.* **13**, 273 (2022).
71. Liu, G. et al. A charge-density-wave oscillator based on an integrated tantalum disulfide–boron nitride–graphene device operating at room temperature. *Nat. Nanotechnol.* **11**, 845–850 (2016).
72. Balandin, A. A., Zaitsev-Zotov, S. V. & Grüner, G. Charge-density-wave quantum materials and devices—new developments and future prospects. *Appl. Phys. Lett.* **119**, 170401 (2021).
73. Wang, W.-S., Li, Z.-Z., Xiang, Y.-Y. & Wang, Q.-H. Competing electronic orders on kagome lattices at van Hove filling. *Phys. Rev. B* **87**, 115135 (2013).
74. O'Brien, A., Pollmann, F. & Fulde, P. Strongly correlated fermions on a kagome lattice. *Phys. Rev. B* **81**, 235115 (2010).
75. Kiesel, M. L., Platt, C. & Thomale, R. Unconventional Fermi surface instabilities in the kagome Hubbard model. *Phys. Rev. Lett.* **110**, 126405 (2013).
76. Haldane, F. D. M. Model for a quantum Hall effect without Landau levels: condensed-matter realization of the parity anomaly. *Phys. Rev. Lett.* **61**, 2015–2018 (1988).
77. Varma, C. M. Non-Fermi-liquid states and pairing instability of a general model of copper oxide metals. *Phys. Rev. B* **55**, 14554–14580 (1997).
78. X-area package (STOE and Cie GmbH, Darmstadt, Germany, 2022).
79. Petricek, V., Dusek, M., Plasil, J. & Palatinus, L. Jana2020—a new version of the crystallographic computing system Jana. *Z. Kristallogr.* **229**, 345–352 (2023).
80. Pallikara, I. et al. The physical significance of imaginary phonon modes in crystals. *Electron. Struct.* **4**, 033002 (2022).
81. Hellman, O. et al. Temperature dependent effective potential method for accurate free energy calculations of solids. *Phys. Rev. B* **87**, 104111 (2013).
82. Monacelli, L. et al. The stochastic self-consistent harmonic approximation: calculating vibrational properties of materials with full quantum and anharmonic effects. *J. Phys.: Condens. Matter* **33**, 363001 (2021).
83. Momma, K. & Izumi, F. VESTA3 for three-dimensional visualization of crystal, volumetric and morphology data. *J. Appl. Crystallogr.* **44**, 1272–1276 (2011).

## Acknowledgements

Z.G. acknowledges support from the Swiss National Science Foundation (SNSF) through the SNSF Starting Grant (No. TMSGI2\_211750). We acknowledge DESY (Hamburg, Germany), a member of the Helmholtz Association HGF, for the provision of experimental facilities. Parts of this research were carried out at the P21.1 beamline. I.P. acknowledges support from Paul Scherrer Institute research grant No. 2021\_01346, and S.S. acknowledges support from the SNSF through grant No. 200021\_188706. I.P. acknowledges Dr. Vladimir Pomjakushin and Prof. Alexander Tsirlin for valuable discussions. The work at Princeton is supported by the U.S. Department of Energy (DOE) Office of Science, the National Quantum Information (NQI) Science Research Centers, the Quantum Science Center

(QSC at ORNL) and by the U.S. DOE under the Basic Energy Sciences program (grant number DOE/BES DE-FG-02-05ER46200). T.N. acknowledges support from the Swiss National Science Foundation through a Consolidator Grant (ITQC, TMC2-2\_213805). This work was partially supported by JST-Mirai Program (JPMJMI20A1), JST-ASPIRE Program (JPMJAP2317). J.C. and J.K. acknowledges support from SNSF grant 200021\_188564.

### Author contributions

Z.G. conceived and designed the project. Z.G. and D.J.G. supervised the project. Growth of  $\text{La}(\text{Ru}_{1-x}\text{Fe}_x)_3\text{Si}_2$  samples: C.M.III and D.J.G. Growth of undoped crystal  $\text{LaRu}_3\text{Si}_2$ : H.N. and S.N. X-ray diffraction experiments at DESY, analysis and corresponding discussions: C.M.III, J.K., I.B., O.I., M.v.Z., J.C., and Z.G. Laboratory single crystal X-ray diffraction experiments and corresponding discussions: I.P., C.M.III, V.P., E.P., S.S., M.M., V.S., A.A., H.L., R.K., D.J.G., and Z.G. X-ray data refinement: I.P. and V.P. DFT calculations and corresponding discussions: Y.Q., G.X., T.N., M.H.F., J.-X.Y., M.Z.H., and Z.G. Differential scanning calorimetry experiments and corresponding discussions: D.J.G., J.N.G., and Z.G. Figure development: Z.G., I.P., C.M.III, and D.J.G. Writing of the paper: Z.G. and I.P. with contributions from all authors. All authors discussed the results, interpretation, and conclusion.

### Competing interests

The authors declare no competing interests.

### Additional information

**Supplementary information** The online version contains supplementary material available at <https://doi.org/10.1038/s42005-024-01673-y>.

**Correspondence** and requests for materials should be addressed to D. J. Gawryluk or Z. Guguchia.

**Peer review information** *Communications Physics* thanks the anonymous reviewers for their contribution to the peer review of this work.

**Reprints and permissions information** is available at <http://www.nature.com/reprints>

**Publisher's note** Springer Nature remains neutral with regard to jurisdictional claims in published maps and institutional affiliations.

**Open Access** This article is licensed under a Creative Commons Attribution 4.0 International License, which permits use, sharing, adaptation, distribution and reproduction in any medium or format, as long as you give appropriate credit to the original author(s) and the source, provide a link to the Creative Commons licence, and indicate if changes were made. The images or other third party material in this article are included in the article's Creative Commons licence, unless indicated otherwise in a credit line to the material. If material is not included in the article's Creative Commons licence and your intended use is not permitted by statutory regulation or exceeds the permitted use, you will need to obtain permission directly from the copyright holder. To view a copy of this licence, visit <http://creativecommons.org/licenses/by/4.0/>.

© The Author(s) 2024